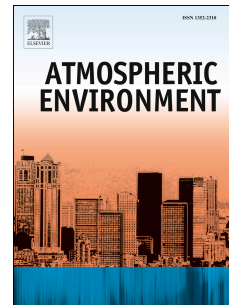




Since January 2020 Elsevier has created a COVID-19 resource centre with free information in English and Mandarin on the novel coronavirus COVID-19. The COVID-19 resource centre is hosted on Elsevier Connect, the company's public news and information website.

Elsevier hereby grants permission to make all its COVID-19-related research that is available on the COVID-19 resource centre - including this research content - immediately available in PubMed Central and other publicly funded repositories, such as the WHO COVID database with rights for unrestricted research re-use and analyses in any form or by any means with acknowledgement of the original source. These permissions are granted for free by Elsevier for as long as the COVID-19 resource centre remains active.

# Journal Pre-proof



NO<sub>2</sub> retrievals from NOAA-20 OMPS: Algorithm, evaluation, and observations of drastic changes during COVID-19

Xinzhou Huang, Kai Yang, Shobha Kondragunta, Zigang Wei, Lucas Valin, James Szykman, Mitch Goldberg

PII: S1352-2310(22)00432-0

DOI: <https://doi.org/10.1016/j.atmosenv.2022.119367>

Reference: AEA 119367

To appear in: *Atmospheric Environment*

Received Date: 29 April 2022

Revised Date: 10 August 2022

Accepted Date: 29 August 2022

Please cite this article as: Huang, X., Yang, K., Kondragunta, S., Wei, Z., Valin, L., Szykman, J., Goldberg, M., NO<sub>2</sub> retrievals from NOAA-20 OMPS: Algorithm, evaluation, and observations of drastic changes during COVID-19, *Atmospheric Environment* (2022), doi: <https://doi.org/10.1016/j.atmosenv.2022.119367>.

This is a PDF file of an article that has undergone enhancements after acceptance, such as the addition of a cover page and metadata, and formatting for readability, but it is not yet the definitive version of record. This version will undergo additional copyediting, typesetting and review before it is published in its final form, but we are providing this version to give early visibility of the article. Please note that, during the production process, errors may be discovered which could affect the content, and all legal disclaimers that apply to the journal pertain.

© 2022 Published by Elsevier Ltd.

**Author Contributions Statement**

**Xinzhou Huang:** Conceptualization, Data curation, Formal analysis, Investigation, Methodology, Software, Validation, Visualization, Roles/Writing - original draft, Writing - review & editing. **Kai Yang:** Conceptualization, Data curation, Funding acquisition, Methodology, Project administration, Resources, Software, Supervision, Writing - review & editing. **Shobha Kondragunta:** Project administration; Resources; Supervision; Writing - review & editing. **Zigang Wei:** Investigation. **Lucas Valin:** Resources, Writing - review & editing. **James Szykman:** Resources, Supervision, Writing - review & editing. **Mitch Goldberg:** Project administration, Resources, Supervision.

1 **NO<sub>2</sub> retrievals from NOAA-20 OMPS: algorithm, evaluation, and observations of**  
2 **drastic changes during COVID-19**

3 **Xinzhou Huang<sup>1</sup>, Kai Yang<sup>1</sup>, Shobha Kondragunta<sup>2</sup>, Zigang Wei<sup>3</sup>, Lucas Valin<sup>4</sup>, James**  
4 **Szykman<sup>5</sup>, Mitch Goldberg<sup>2</sup>**

5 <sup>1</sup>Department of Atmospheric and Oceanic Science, University of Maryland, College Park, MD,  
6 USA.

7 <sup>2</sup>NOAA NESDIS, College Park, MD, USA

8 <sup>3</sup>IMSG at NOAA, College Park, MD, USA.

9 <sup>4</sup>US EPA, ORD, Center for Environmental Measurements and Modeling, Research Triangle  
10 Park, NC, USA.

11 <sup>5</sup>US EPA, ORD, Center for Environmental Measurements and Modeling, Hampton, VA, USA.

12  
13 Corresponding author: Kai Yang ([kaiyang@umd.edu](mailto:kaiyang@umd.edu))

14  
15 **Keywords:**

16 NOAA-20; OMPS; stratosphere and troposphere NO<sub>2</sub>; COVID-19  
17  
18

## 19 **Abstract**

20 We present the first NO<sub>2</sub> measurements from the Nadir Mapper of Ozone Mapping and Profiler  
21 Suite (OMPS) instrument aboard the NOAA-20 satellite. NOAA-20 OMPS was launched in  
22 November 2017, with a nadir resolution of  $17 \times 13 \text{ km}^2$  similar to the Ozone Monitoring  
23 Instrument (OMI). The retrieval of NOAA-20 NO<sub>2</sub> vertical columns were achieved through the  
24 Direct Vertical Column Fitting (DVCF) algorithm, which was uniquely designed and  
25 successfully used to retrieve NO<sub>2</sub> from OMPS aboard Suomi National Polar-orbiting Partnership  
26 (SNPP) spacecraft, predecessor to NOAA-20. Observations from NOAA-20 reveal a 20 - 40%  
27 decline in regional tropospheric NO<sub>2</sub> in January-April 2020 due to COVID-19 lockdown,  
28 consistent with the findings from other satellite observations. The NO<sub>2</sub> retrievals are  
29 preliminarily validated against ground-based Pandora spectrometer measurements over the New  
30 York City area as well as other U.S. Pandora locations. It shows OMPS total columns tend to be  
31 lower in polluted urban regions and higher in clean areas/episodes associated with relatively  
32 small NO<sub>2</sub> total columns, but generally the agreement is within  $\pm 2.5 \times 10^{15}$  molecules/cm<sup>2</sup>.  
33 Comparisons of stratospheric NO<sub>2</sub> columns exhibit the excellent agreement between OMPS and  
34 OMI, validating OMPS capability in capturing the stratospheric background accurately. These  
35 results demonstrate the high sensitivity of OMPS to tropospheric NO<sub>2</sub> and highlight its potential  
36 use for extending the long-term global NO<sub>2</sub> record.

## 37 **1 Introduction**

38 Nitrogen dioxide (NO<sub>2</sub>) is a major air pollutant in the troposphere with varying levels of  
39 regulatory standards for ambient concentrations across the world. Its prevalence contributes to  
40 other secondary air pollutant formation, such as tropospheric ozone and nitrate aerosols, which

41 are consequently harmful to human health and climate (Lelieveld et al., 2015; Seinfeld and  
42 Pandis, 2016). The primary sources of nitrogen oxides ( $\text{NO}_x = \text{NO}_2 + \text{NO}$ ) are anthropogenic,  
43 produced mostly by combustion processes, with the rest being natural sources from fires,  
44 lightning, and soils. Due to the short photochemical lifetime of  $\text{NO}_2$ , which varies from ~2-6 hr  
45 in summer to ~12-27 hr in winter (Beirle et al., 2011; Laughner and Cohen, 2019; Shah et al.,  
46 2020), tropospheric  $\text{NO}_2$  concentrations are spatially correlated with local  $\text{NO}_x$  emissions at  
47 spatial scales of ~10 km (Beirle et al., 2019). The atmospheric chemistry community has been  
48 using satellite observations since the mid-1990s to monitor daily global  $\text{NO}_2$  loading, investigate  
49 long-term trends and short-term  $\text{NO}_2$  changes, and locate  $\text{NO}_x$  emission sources to aid control  
50 policy strategies (Duncan et al., 2016; Lin et al., 2019).

51 The ongoing COVID-19 pandemic has caused unprecedented societal and economic impact  
52 worldwide. Satellite observations show a drastic decline in tropospheric  $\text{NO}_2$  vertical column  
53 density over China following the outbreak of COVID-19, reflecting reduced fossil fuel usage due  
54 to decreases in economic activity and restrictions on travel (Huang and Sun, 2020; Liu et al.,  
55 2020). Similar declines have also been seen over Italy (Bauwens et al., 2020), India (ESA, 2020),  
56 North America (Goldberg et al., 2020; Kondragunta et al., 2021; Tzortziou et al., 2021) as  
57 observed by the TROPOspheric Monitoring Instrument (TROPOMI) and the Ozone Monitoring  
58 Instrument (OMI). These satellite-based studies illustrate the importance of spaceborne  
59 observations for providing timely and continuous air quality monitoring.

60 The OMPS Nadir Mapper aboard the NOAA-20 satellite was launched in November 2017,  
61 which is a successor to OMPS aboard Suomi National Polar-orbiting Partnership (SNPP) satellite  
62 under the NOAA/NASA Joint Polar Satellite Systems (JPSS) mission. The JPSS mission  
63 provides OMPS in orbit to the 2040s, extending the long-term record of many atmospheric trace

64 gases, including O<sub>3</sub>, SO<sub>2</sub> and, NO<sub>2</sub>. OMPS as an independent measurement also plays a critical  
65 role in the global satellite constellation by providing a means of inter-calibrating and cross-  
66 validating with other satellite instruments (Judd et al., 2018). With the COVID-19 crisis, there is  
67 broad interest in accurate assessments of regional NO<sub>2</sub> column changes from multi-satellite  
68 platforms. The development of the first NOAA-20 OMPS NO<sub>2</sub> product describe herein was  
69 established after the emergence of the COVID-19 pandemic. In this study, we present the first  
70 results of NOAA-20 OMPS NO<sub>2</sub> with applications during the COVID-19 pandemic. We compare  
71 OMPS NO<sub>2</sub> retrievals with NO<sub>2</sub> columns retrieved from OMI and ground-based Pandora  
72 spectrometer measurements. Our results demonstrate OMPS capability in detecting spatial and  
73 temporal changes of tropospheric NO<sub>2</sub> air pollution.

74

## 75 **2 NO<sub>2</sub> from NOAA-20**

### 76 2.1 NOAA-20 OMPS Instrument Overview

77 OMPS Nadir Mapper (NM) is a nadir-viewing hyperspectral instrument that measures  
78 backscattered ultraviolet (UV) radiance spectra. The NOAA-20 OMPS spacecraft  
79 launched in November 2017, is the second of several OMPS missions planned for the  
80 next decade and beyond on the NOAA/NASA JPSS spacecrafts, with the first OMPS  
81 mission launched in October 2011, aboard SNPP spacecraft. Similar to SNPP, NOAA-20  
82 is in a Sun-synchronous orbit with a local ascending (northbound) equator crossing-time  
83 at 1:30 P.M., close in time to the Aura/OMI & TROPOMI overpasses at 1:45 P.M. local  
84 time (Table 1). NOAA-20 OMPS has a spatial resolution of  $17 \times 13 \text{ km}^2$  at nadir,

85 improved over the nadir resolution of  $50 \times 50 \text{ km}^2$  of SNPP OMPS, and OMPS  
 86 resolution will be continually improved on the subsequent JPSS satellites.

87 NOAA-20 OMPS measures UV radiance in the 300-420 nm wavelength range at a  
 88 spectral resolution of 1 nm and a sampling rate of 0.42 nm per pixel. Although NOAA-20  
 89 OMPS extends the spectral coverage to 420 nm (compared to SNPP OMPS in the 300-  
 90 380 nm range), its radiance quality is poor for wavelength longer than 390 nm and thus  
 91 not used for  $\text{NO}_2$  retrieval, and the shorter wavelength spectra ( $< 345 \text{ nm}$ ) are strongly  
 92 affected by ozone absorption. Therefore, the 345-390 nm wavelength range was utilized  
 93 for OMPS  $\text{NO}_2$  retrieval, shorter in wavelength than other legacy UV/VIS instruments  
 94 (Table 1). We adopted the Direct Vertical Column Fitting (DVCF) technique to retrieve  
 95  $\text{NO}_2$  from NOAA-20 OMPS-NM UV radiance, which is the algorithm currently  
 96 implemented in the operational SNPP OMPS  $\text{NO}_2$  product (Yang et al., 2014). Details  
 97 about the DVCF algorithm and challenges for  $\text{NO}_2$  retrievals in the UV spectra are  
 98 elucidated in section 2.2.

99 **Table 1.** Comparison of satellite  $\text{NO}_2$  instruments on Low Earth Orbit, including OMI,  
 100 SNPP OMPS, NOAA-20 OMPS and TROPOMI.

	OMI	SNPP OMPS	NOAA-20 OMPS	TROPOMI
Spectral window	405 – 465 nm	345 – 380 nm	345 – 390 nm	405 – 465 nm
Spectral resolution	0.63 nm	1 nm	1 nm	0.63 nm
Swath width	2600 km	2800 km	2800 km	2600 km
FOV	75°	110°	110°	75°
Signal-to-noise ratio	1200	2500	600-800 <sup>1</sup>	1200
Nadir resolution	$24 \times 13 \text{ km}^2$	$50 \times 50 \text{ km}^2$	$13 \times 17 \text{ km}^2$	$5.5 \times 3.5 \text{ km}^2$
Overpassing time	13:45 LT	13:30 LT	13:30 LT	13:45 LT



101 <sup>1</sup> Note that the signal-to-noise ratio of NOAA-20 OMPS is estimated to be about  $1/\sqrt{11}$  of that of SNPP  
 102 OMPS.

103

## 104 2.2 DVCF retrieval algorithm

105 The Direct Vertical Column Fitting (DVCF) algorithm is applied to the NOAA-20 OMPS-  
 106 NM spectral measurements to retrieve the atmospheric NO<sub>2</sub> vertical columns. The  
 107 approach of this algorithm is to find retrieved parameters so that the modeled radiance  
 108 spectra ( $I_{TOA}$ ) match the satellite-measured spectra ( $I_m$ ). Algebraically, radiance  
 109 matching is accomplished by minimizing the cost function  $\left\| \Delta \mathbf{y} \mathbf{S}_y^{-\frac{1}{2}} \right\|^2$ , where  $\mathbf{S}_y$  is the  
 110 measurement error covariance matrix and  $\Delta \mathbf{y} = \{\ln I_m - \ln I_{TOA}\}$  is the residual vector  
 111 for all wavelengths in a spectral window, one of which at wavelength  $\lambda$  can be written as:

$$\begin{aligned}
 112 \quad \Delta y(\lambda) = & V \int_0^\infty \frac{\partial \ln I_{TOA}(\lambda)}{\partial \tau_z} S_z \sigma(\lambda, T_z) dz - \sum_{i=1}^m \xi_i \sigma_i(\lambda, T_i) \\
 113 \quad & + \sum_{k=0}^{n=1} \frac{\partial \ln I_{TOA}(\lambda)}{\partial R} \Delta R_k (\lambda - \lambda_0)^k + \varepsilon \quad (1)
 \end{aligned}$$

114 The least-square solution to the set of Eq. (1) described the retrieval of NO<sub>2</sub> vertical  
 115 column ( $V$ ) as a process of fitting the residuals with the vertical column weighting  
 116 function (WF, i.e.  $\int_0^\infty \frac{\partial \ln I_{TOA}}{\partial \tau_z} S_z \sigma(T_z) dz$ ) and the slant columns  $\{\xi_i, i = 1 \dots m\}$  of other  
 117 trace gases (including O<sub>3</sub>, HCHO, BrO, and OCIO, thus  $m = 4$ ) with their molecular  
 118 absorption cross sections  $\{\sigma_i(T_i), i = 1 \dots m\}$  at their respective temperature  $\{T_i, i =$   
 119  $1 \dots m\}$ .  $S_z$  is the shape factor, which is the normalized vertical profile;  $T_z$  is the

120 atmospheric temperature, a function of altitude ( $z$ ); and  $\epsilon$  is the total error, which includes  
 121 satellite measurement error and the forward modeling uncertainty. Here,  $\tau_z$  is the optical  
 122 thickness of an infinitesimally thin layer at  $z$ , and the total absorption optical  
 123 thickness ( $\tau$ ) is the integration of  $\tau_z$ :  $\tau = \int_0^\infty \tau_z dz = V \int_0^\infty \sigma(T_z) S_z dz$ . The radiance  
 124 matching is primarily through adjusting the reflectivity parameters  $\{R_k, k = 0 \dots n\}$ , which  
 125 specify the Mixed Lambert-Equivalent Reflectivity (MLER) model. Here  $n=1$  describes  
 126 the reflectivity change linearly with wavelength, a simplified treatment to account for  
 127 aerosol effects. The spectral structures in the measured spectra are then reproduced by  
 128 finding the correct vertical column ( $V$ ) and other absorbers slant columns ( $\xi_i$ ).

129 After the direct retrieval of total vertical columns ( $V$ ) as described in Eq. (1), OMPS  
 130 stratospheric and tropospheric  $\text{NO}_2$  vertical columns are separated using an orbit-based  
 131 sliding median correction approach. The basic premise behind Stratosphere-Troposphere  
 132 Separation (STS) is that the spatial distribution of stratospheric  $\text{NO}_2$  is more  
 133 homogeneous than that of tropospheric  $\text{NO}_2$  due to the localized anthropogenic emission  
 134 and short lifetime of the latter. The sliding median STS technique used in NOAA-20  
 135 OMPS retrieval was first developed for  $\text{SO}_2$  retrieval in OMI (Yang et al., 2009, 2007),  
 136 and then applied in  $\text{NO}_2$  retrieval in SNPP OMPS (Yang et al., 2014). It follows a simple  
 137 procedure: first, retrieved total vertical columns are partitioned into stratospheric ( $V_s^i$ ) and  
 138 tropospheric components using tropopause inputs and the a priori shape factors. Second,  
 139 the initial stratospheric columns get refined by locating and smoothing out the high-  
 140 frequency structures that are attributed to the inaccuracies in a priori shape factors.  
 141 Specifically, two empirical latitudinal bands (e.g.,  $2^\circ$  and  $20^\circ$ , subject to modifications in  
 142 certain conditions) are used to construct two smoothed stratospheric fields from the initial

143 field along the orbital track for each cross-track position of a satellite orbit using the  
 144 sliding median method, as detailed in (Yang et al., 2014). The smaller latitude band is  
 145 used to generate a higher-frequency smoothed field ( $\mathbf{m}_h$ ) that retains possible  
 146 tropospheric signals, while the larger band is used to construct a lower-frequency  
 147 smoothed field ( $\mathbf{m}_l$ ) with minimal tropospheric contributions that is representative of  
 148 background median values. Thus, the excesses (+) and deficits (-) of stratospheric NO<sub>2</sub>  
 149 are obtained from the difference between the two smoothed fields ( $\mathbf{m}_h - \mathbf{m}_l$ ). The  
 150 corrected stratospheric NO<sub>2</sub> column is then adjusted as  $\mathbf{V}_s = \mathbf{V}_s^l - (\mathbf{m}_h - \mathbf{m}_l)$ . After the  
 151 stratospheric vertical columns are consolidated, finally, the corresponding tropospheric  
 152 NO<sub>2</sub> columns ( $\mathbf{V}_t$ ) are retrieved by solving a new set of linear equations:

$$\begin{aligned}
 153 \quad & \ln \frac{I_m(\lambda)}{I_{TOA}(\lambda)} + V_s \int_{Z_{tp}}^{\infty} \mathbf{m}_z(\lambda) S_z \sigma(\lambda, T_z) dz + \sum_i \xi_i \sigma_i(\lambda, T_i) \\
 154 \quad & - \sum_{k=0}^n \frac{\partial \ln I_{TOA}(\lambda)}{\partial R} \Delta R_k (\lambda - \lambda_0)^k \\
 155 \quad & = -V_t \int_0^{Z_{tp}} \mathbf{m}_z(\lambda) S_z \sigma(\lambda, T_z) dz + \varepsilon \quad (2)
 \end{aligned}$$

156 , where  $Z_{tp}$  is the tropopause altitude. This completes the whole process of DVCF  
 157 retrieval of OMPS tropospheric and stratospheric NO<sub>2</sub> vertical columns.

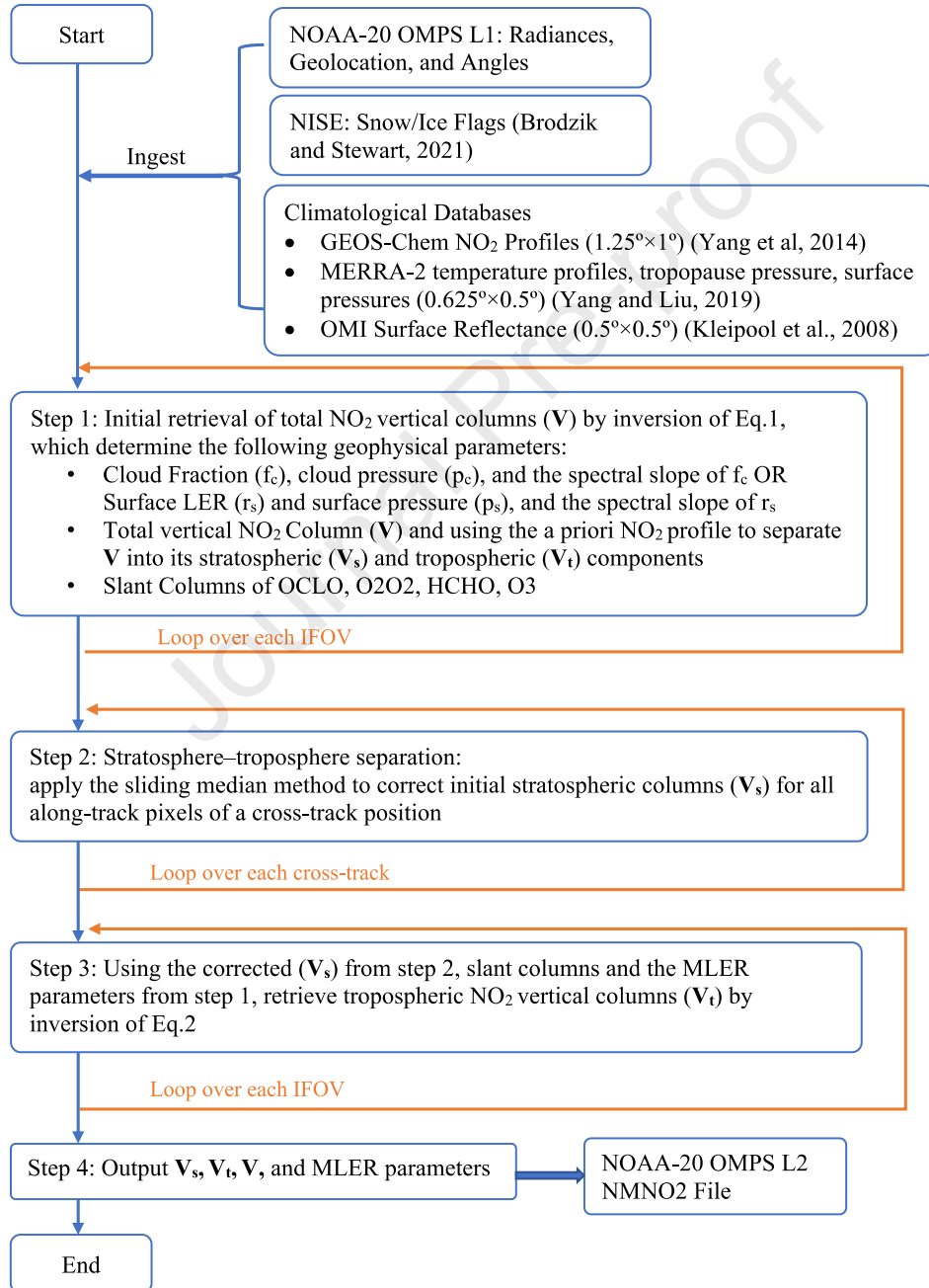
158 The key improvement of the DVCF algorithm over the traditional Differential Optical  
 159 Absorption Spectroscopy (DOAS) approach lies in the more accurate representation of  
 160 NO<sub>2</sub> measurement sensitivity, and thus more accurate NO<sub>2</sub> retrieval. In UV, the Rayleigh  
 161 scattering from air molecules is quite strong and varies with wavelength drastically ( $\sim 1/\lambda$   
 162 <sup>4</sup>). Consequently, the tropospheric air mass factors (AMFs) depend on the wavelength

163 significantly. The spectrally dependent WF used in the DVCF captures the measurement  
164 sensitivity more accurately than the single-wavelength AMFs employed in the DOAS  
165 algorithm. Furthermore, retrieving surface reflectance or cloud fraction from the same  
166 spectral range, instead of taking it from ancillary inputs, such as climatological values or  
167 measurements from different spectra, improves the quantification of measurement  
168 sensitivity. Both improvements enable better spectral fits to the measured spectra and  
169 provide more accurate vertical column weighting functions, and thus allows more  
170 accurate and precise retrievals of NO<sub>2</sub> vertical columns than the traditional DOAS  
171 approach. Typically, the DOAS retrieval from UV spectra underestimates heavy NO<sub>2</sub>  
172 pollutions (> 2 DU) in the boundary layer by more than 10% compared to the  
173 corresponding DVCF retrieval.

174 With the theoretical background of the DVCF algorithm, here we summarize the  
175 algorithmic procedure applied to NOAA-20 Level-1 (L1) data to produce the Level-2

176 (L2) NO<sub>2</sub> product in the flowchart Algorithm 1, including references to the input  
 177 ancillary and climatological data.

178 Algorithm 1. Flowchart that shows the processing of NOAA-20 OMPS by the DVCF  
 179 algorithm.



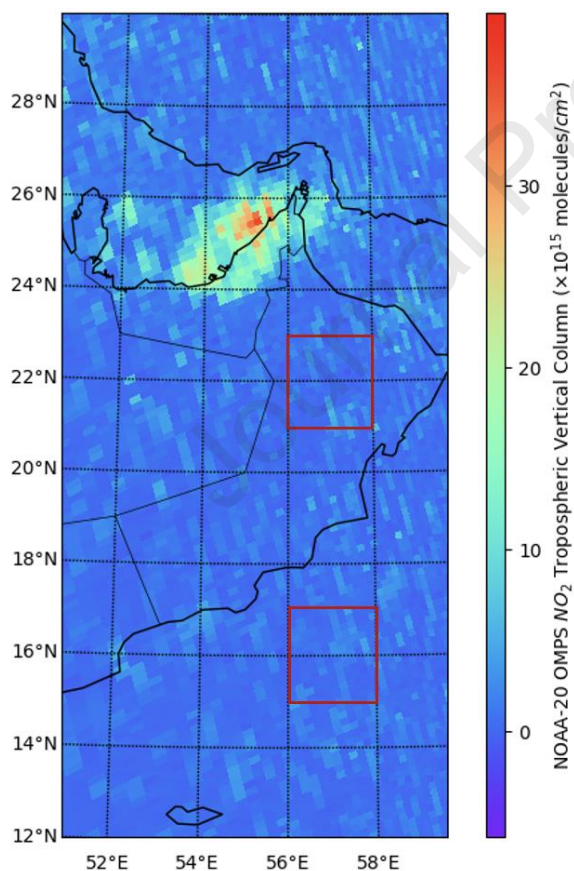
180

181 2.3 Measurement sensitivity of NOAA-20 OMPS NO<sub>2</sub>

182 The precision (sensitivity) of a satellite instrument is often assessed over remote areas,  
183 where the measurement variability is dominated by random errors originating from  
184 measurement noise. The measurement sensitivity of NOAA-20 OMPS NO<sub>2</sub> tropospheric  
185 vertical column densities (TVCDs) over remote ocean (Indian Ocean) and remote desert  
186 (Arabian Peninsula) are  $0.5 \times 10^{15}$ ,  $0.7 \times 10^{15}$  molecules/cm<sup>2</sup>, respectively. The values  
187 are 1  $\sigma$  (standard deviation) of the directly retrieved tropospheric NO<sub>2</sub> vertical columns  
188 (Figure 1). We adopted the same method used to quantify OMI NO<sub>2</sub> sensitivity as  
189 demonstrated in (Boersma et al., 2007; Valin et al., 2011). The areas selected to report  
190 OMPS sensitivity are 2° by 2° boxes between 56°E and 58°E, the box for the remote  
191 desert over Arabian Peninsula is between 21°N and 23°N, and the box for the remote  
192 Indian ocean is between 15°N and 17°N (Figure 1). It is worth noting that we used  
193 vertical columns to report sensitivity instead of the slant columns as used by ref. (Valin et  
194 al., 2011) because the OMPS DVCF retrieval algorithm retrieves the vertical columns  
195 directly from a spectral fit to the Earth reflectance spectrum. In other words, the slant  
196 column is a derived quantity from the vertical column retrieval. Therefore, it makes more  
197 sense to use vertical columns to characterize OMPS sensitivity. For OMI, since slant  
198 columns are determined with spectral fit in the first step of the DOAS retrieval algorithm,  
199 it is better to use slant column to quantify OMI sensitivity.

200 The sensitivity of SNPP OMPS NO<sub>2</sub> TVCDs is  $0.4 \times 10^{15}$  molecules/cm<sup>2</sup> (Yang et al.,  
201 2014), better than NOAA-20 OMPS. Although the two products are built on the same  
202 retrieval system, the NOAA-20 NO<sub>2</sub> is noisier than SNPP primarily because the NOAA-  
203 20 OMPS instrument has a smaller signal-to-noise ratio (SNR) than its predecessor SNPP

204 OMPS (Table 1). Since SNPP OMPS has bigger pixel size ( $50 \times 50 \text{ km}^2$ ) than NOAA-20  
205 OMPS ( $17 \times 13 \text{ km}^2$ ), if we were to estimate NOAA-20 SNR from SNPP, we can  
206 aggregate 11 NOAA-20 pixels into 1 SNPP pixel to make NOAA-20 equivalent to SNPP.  
207 This aggregation process cancels out noise but keeps the signal, which means that the  
208 NOAA-20 SNR is about  $\sqrt{11} \sim 3.32$  times lower than SNPP. Therefore, NOAA-20  
209 OMPS measurement sensitivity is intrinsically limited by its smaller signal-to-noise ratio  
210 and the DVCF retrieval algorithm is specially designed to amplify its measurement  
211 sensitivity as possible.



212

213 **Figure 1.** NOAA-20 OMPS  $\text{NO}_2$  tropospheric vertical columns over the Eastern Arabian  
214 Peninsula on 10 November 2019. The scan time on the map is 09:00 to 09:05 UTC. The

215 sensitivity of NOAA-20 tropospheric NO<sub>2</sub> columns is reported over the remote ocean and  
216 desert, where red boxes indicate.

217

### 218 **3 Results**

#### 219 3.1 Stratospheric NO<sub>2</sub>: comparison with OMI

220 Before evaluating NOAA-20 tropospheric NO<sub>2</sub> retrievals, we first examine the  
221 stratospheric NO<sub>2</sub> observations from NOAA-20, since the stratospheric columns  
222 represent the clean background values over which tropospheric NO<sub>2</sub> enhancements are  
223 detected. We compared the seasonal averaged NO<sub>2</sub> stratospheric vertical column densities  
224 (SVCDs) observed from NOAA-20 OMPS and OMI in Figure 2. The daily NO<sub>2</sub> SVCDs  
225 (Level-2 data) collected from the two instruments were zonally averaged using 2° latitude  
226 bins for all cross-track iFOVs (OMI row anomaly affected pixels are excluded), and the  
227 seasonal averaged SVCDs were then plotted as a function of latitude. Since OMPS and  
228 OMI have similar overpassing time, the observed SVCDs are compared directly without  
229 photochemical corrections to compensate for NO<sub>2</sub> diurnal cycles (Rivas et al., 2014). In  
230 all seasons, the stratospheric NO<sub>2</sub> field is characterized by a tropical minimum over the  
231 equatorial NO<sub>y</sub> (odd nitrogen) production zone, where total nitrogen is subject to upward  
232 and poleward transport. Outside the tropical regions, the stratospheric NO<sub>2</sub> field is  
233 characterized by a winter minimum and a summer maximum. The seasonal evolution of  
234 stratospheric NO<sub>2</sub> is explained by the sunlight-driven exchange between NO<sub>x</sub> (nitrogen  
235 oxides) and other reservoir oxidized nitrogen species: N<sub>2</sub>O<sub>5</sub> (primarily), HNO<sub>3</sub> and  
236 ClONO<sub>2</sub>. As the amount of daily photolysis decreases over winter, NO<sub>x</sub> begins to store

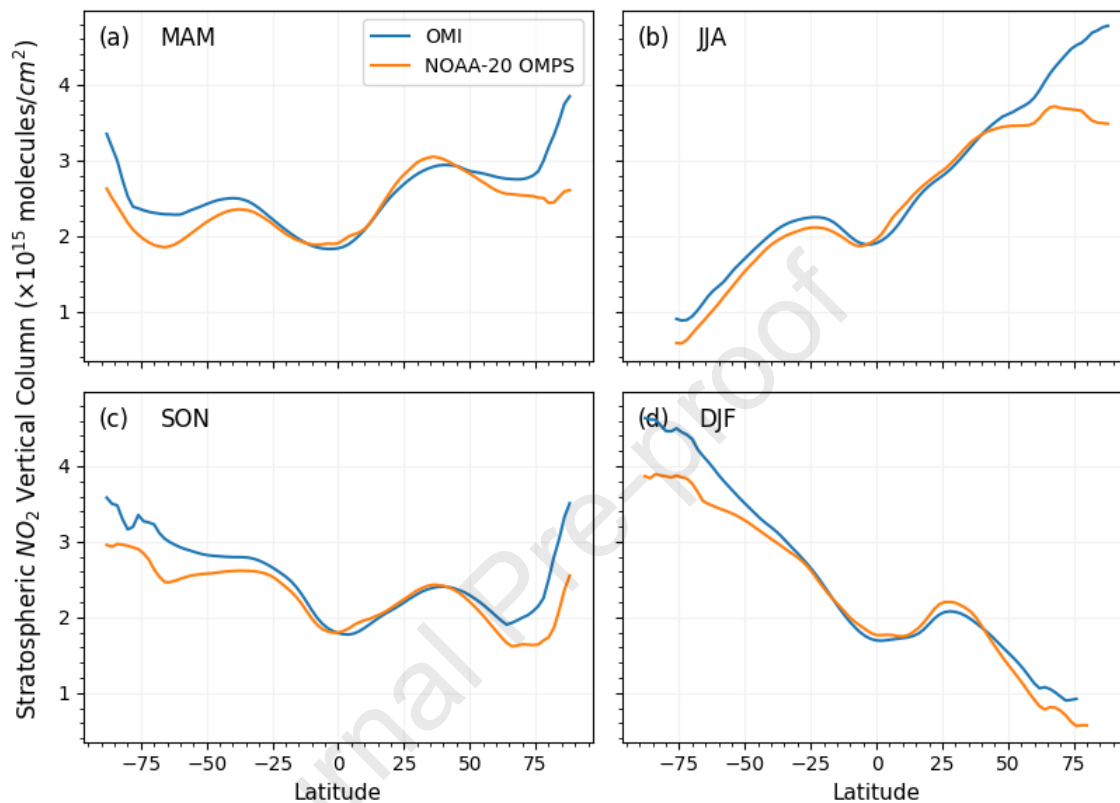


237 into inactive  $\text{N}_2\text{O}_5$  reservoirs, which results in a decrease of  $\text{NO}_x$  columns (Solomon and  
238 Garcia, 1983). Conversely, as the solar angle decreases in summer, the photolytic release  
239 of reservoir species increases  $\text{NO}_2$  columns.

240 OMI and NOAA-20 OMPS retrievals of stratospheric  $\text{NO}_2$  columns over the tropics and  
241 mid-latitude are very similar (Figure 2). In high latitudes, the differences are larger. This  
242 is primarily due to the sunlight driven  $\text{NO}_2$  diurnal variations at large solar zenith angles  
243 (SZA). The large SZA at higher latitude is more prone to the sharp  $\text{NO}_2$  gradient at day-  
244 night transition, making direct column comparisons more difficult. In addition, large SZA  
245 increases the uncertainty in satellite retrieval of the  $\text{NO}_2$  total columns due to stronger  
246 absorption in the stratosphere and lower signal-to-noise ratio. Studies found that the  
247 differences between satellite- and ground-based  $\text{NO}_2$  measurements are generally larger  
248 for SZA above  $45^\circ$  (Ialongo et al., 2020). We have compared OMI cross-track positions  
249 that are not affected by row anomaly against the equivalent OMPS cross-track positions  
250 based on similar view zenith angle. We find that the row anomaly caused sampling  
251 mismatch are not the main reason for the large discrepancy at high latitudes.

252 OMPS and OMI stratospheric  $\text{NO}_2$  columns show an agreement with  $r = 0.96$  and  
253 average relative difference = -3% for the region between  $65^\circ\text{S}$  and  $65^\circ\text{N}$ . The excellent  
254 agreement between NOAA-20 OMPS and OMI stratospheric columns is promising given  
255 that each relies on independent measurements and very different retrieval methodologies.

256 Also, since stratospheric NO<sub>2</sub> is homogeneously distributed, this comparison is not  
257 subject to instrumental resolution difference.



258  
259 **Figure 2.** Seasonal averaged stratospheric NO<sub>2</sub> vertical columns observed from NOAA-  
260 20 OMPS (orange curve) and OMI (blue curve) as a function of latitude for (a) MAM, (b)  
261 JJA, (c) SON, (d) DJF, over the period from 2019-03-01 to 2020-04-30. OMPS and OMI  
262 show excellent agreement with  $r = 0.96$  and mean relative difference = -3% for the region

263 between 65°S and 65°N. OMI pixels affected by row anomaly are excluded in the  
264 comparison.

265

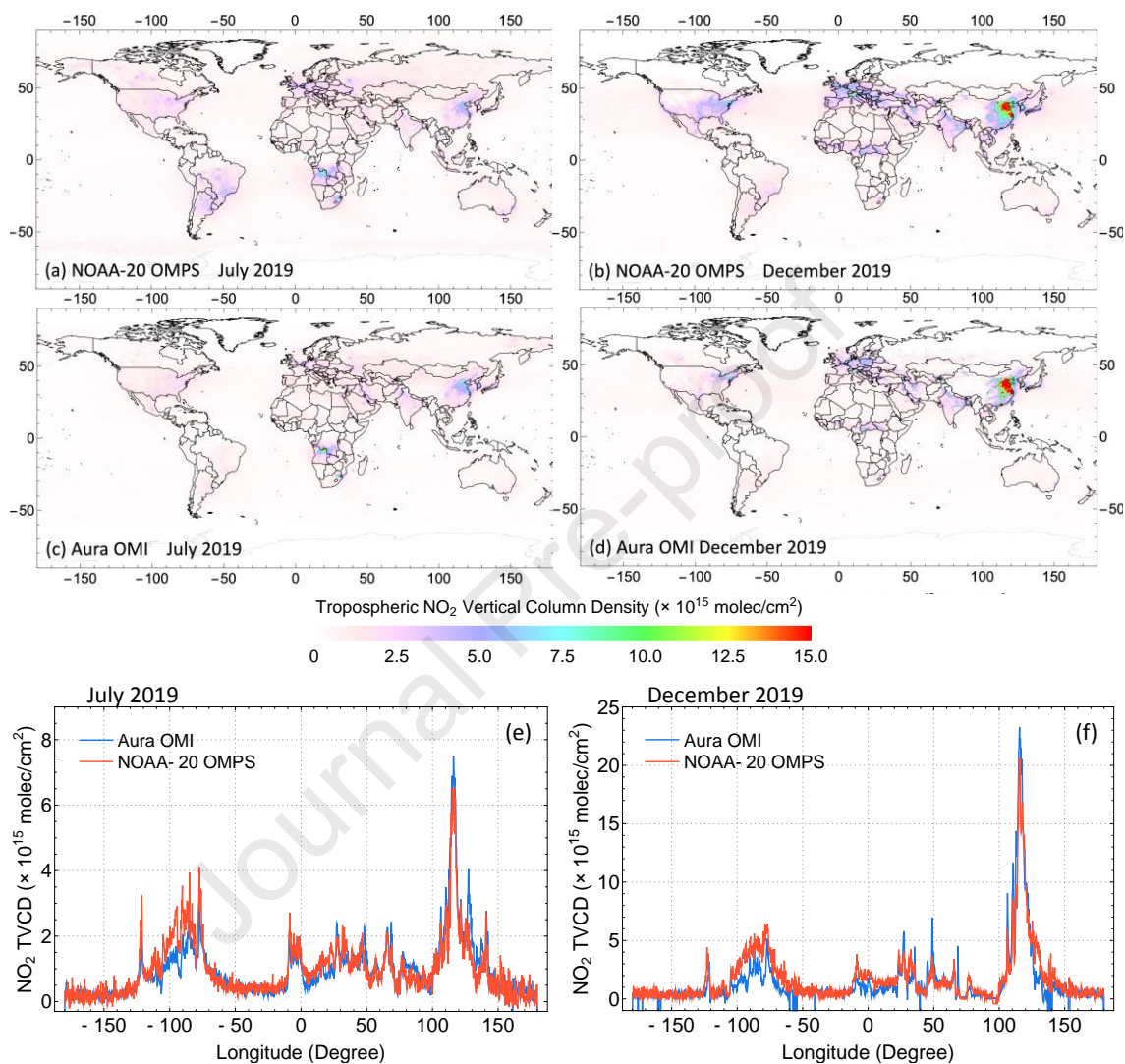
### 266 3.2 Tropospheric NO<sub>2</sub>: comparison with OMI

267 Figure 3 shows maps of the gridded monthly mean NO<sub>2</sub> tropospheric vertical column  
268 densities (TVCDs) derived from NOAA-20 OMPS and OMI for July and December  
269 2019. OMPS monthly mean NO<sub>2</sub> TVCDs are derived from OMPS Level-2 data and are  
270 compared directly with OMI monthly mean columns derived from OMI Level-2 data  
271 using identical gridding procedure. OMI and OMPS data are both gridded at 0.25° ×  
272 0.25° resolution, with the same cloud screening applied: iFOVs (pixels) with radiative  
273 cloud fraction > 30% are excluded. OMI data affected by the row anomaly are also  
274 excluded. We computed OMPS and OMI monthly averages from respective Level-2 data  
275 in the following procedure: the value at each grid cell (0.25° × 0.25°) is determined by  
276 the weighted mean of the qualifying iFOVs that have overlap with the grid cell over the  
277 month. The weight is an observation coverage, defined as the ratio of GridCell-iFOV  
278 overlapping area to the iFOV area. The gridding strategy is often called ‘oversampling’  
279 over a long temporal window, and we use the same gridding method to generate OMPS  
280 Level-3 data and calculate mean NO<sub>2</sub> TVCDs over the designated periods in Section 3.4.

281 The monthly maps provide perspectives of where persistent tropospheric NO<sub>2</sub>  
282 enhancements are located. Places like the United States East Coast, western Europe, East  
283 Asia, and northern India exhibit elevated NO<sub>2</sub> pollution, are the world’s major industrial  
284 and densely populated regions. Both OMPS and OMI observe these NO<sub>2</sub> enhancements.

285 To highlight the similarities and differences between the two NO<sub>2</sub> products, we plot the  
286 longitudinal variations of OMPS and OMI measurements in July and December 2019  
287 mean TVCDs across 38.625°N, where the highest OMI monthly mean value is found in  
288 December 2019 (Figure 3e, f). The NO<sub>2</sub> TVCDs from OMPS and OMI agree very well  
289 over China (between 100° and 140°) at this latitude, but OMPS TVCDs are higher than  
290 OMI over the U.S. (between -100° and -60°) and Europe (between -10° and 20°). These  
291 differences are likely due to different a priori profile assumptions over these regions. The  
292 a priori NO<sub>2</sub> profile used in the current NOAA-20 NO<sub>2</sub> product are taken from the  
293 monthly mean profiles of a 2012 GEOS-Chem global simulation at a coarse resolution  
294 (1° latitude × 1.25° longitude). These a priori profiles describe a much higher boundary  
295 layer NO<sub>2</sub> concentrations than those of the more recent years. A higher boundary layer  
296 NO<sub>2</sub> in the a priori shape factors would result in higher NO<sub>2</sub> column retrievals. This  
297 potentially cause the higher OMPS column NO<sub>2</sub> retrievals than OMI in the U.S. and  
298 Europe. On the other hand, for China, although more recent-year a priori profiles might  
299 reflect lower NO<sub>2</sub> concentrations benefited from environmental regulations, there is still  
300 relatively large abundance of anthropogenic emissions near the surface compared to  
301 upper altitudes and thus the NO<sub>2</sub> vertical distributions (i.e., profile shapes) are not  
302 expected to change much. Therefore, the current agreement between OMPS and OMI in  
303 China would probably sustain in more recent-year a priori profiles. We are developing  
304 new a priori NO<sub>2</sub> profiles that are more appropriate for the current pollution levels to  
305 address the potential errors from inaccurate profile assumptions in the retrievals. Overall,  
306 the similar spatial patterns and good quantitative agreement demonstrate the high

307 tropospheric NO<sub>2</sub> measurement sensitivity of NOAA-20 OMPS that is comparable to  
 308 OMI.



309  
 310 **Figure 3.** Monthly averages of NO<sub>2</sub> tropospheric vertical column densities (TVCDs)  
 311 observed by (a, c) NOAA-20 OMPS for July 2019 and (b, d) OMI for December 2019,  
 312 pixels with cloud fraction of 30% and above are excluded. (e, f) Quantitative comparison

313 of NOAA-20 OMPS and OMI monthly averaged NO<sub>2</sub> TVCDs at 38.625°N, from 180°W  
314 to 180°E.

315

### 316 3.3 Evaluating total NO<sub>2</sub> column with Pandora ground-based observations

317 The accuracy of NOAA-20 OMPS NO<sub>2</sub> columns measurements was preliminarily  
318 evaluated against Pandora ground-based observations over the continental United States  
319 (U.S.) during the period from 2019-02-14 to 2020-04-30 (Figure 5). Pandora instruments  
320 can retrieve NO<sub>2</sub> vertical column densities (VCDs) through two viewing geometries,  
321 either direct-sun or zenith sky. For the time of interest, 13 Pandora instruments operated  
322 in direct-sun mode over the U.S. are compared to NOAA-20 OMPS column  
323 measurements. The direct-sun mode Pandora instruments provide high-quality reference  
324 measurements for evaluating trace gas retrievals from satellite sensors due to their low  
325 uncertainties in AMFs (Judd et al., 2020). The ground stations used in this analysis cover  
326 a variety of atmospheric environments, including 4 Pandoras located in the New York  
327 City (NYC) region: Manhattan NY-CCNY, Queens NY, Bronx NY, and Bayonne NJ  
328 (Figure 4b), and 9 other Pandoras located over mid-Atlantic and western U.S. states,  
329 representing urban/suburban/remote atmospheric conditions (Figure 5). All the sites are  
330 operated as part of the Pandonia Global Network (PGN; [www.pandonia-global-](http://www.pandonia-global-network.org)  
331 [network.org](http://www.pandonia-global-network.org)). Only high-quality Pandora measurements with a quality flag of 0 or 10  
332 were included in this analysis.

333 For the comparison between OMPS and Pandora NO<sub>2</sub> total vertical columns, we adopted  
334 the following coincidence criteria: 1) the average Pandora total NO<sub>2</sub> VCDs are calculated

335 within  $\pm 30$  min of OMPS overpass, and 2) all OMPS data have radiative cloud fractions  
 336 less than 30%. The coincidence criteria are similar to those used in other validation  
 337 studies (Ialongo et al., 2016; Judd et al., 2019). We calculated the linear regression  
 338 statistics using Reduced Major Axis regression with correlation coefficient. This  
 339 regression is chosen over Ordinary Least Square to recognize the potential  
 340 errors/uncertainties in both evaluated and reference measurements. Note that the  
 341 Ordinary Least Square statistics is also provided as a reference in Table 2. The difference  
 342 and relative difference of the two column measurements are also calculated and analyzed,  
 343 and are calculated in the following convention:

$$344 \quad \text{column difference} = \text{OMPS measurement} - \text{Pandora measurement} \quad (3)$$

$$345 \quad \text{relative difference (\%)} = \frac{\text{column difference}}{\text{Pandora measurement}} \times 100\% \quad (4)$$

346 Figure 4a shows the scatter plot and linear regression statistics of OMPS and Pandora  
 347 NO<sub>2</sub> total columns coincidences from 4 sites over NYC area (N = 283). NOAA-20 OMPS  
 348 has an average low bias of 28% (median relative difference, Figure S1b) and is  
 349 moderately correlated ( $r = 0.45$ ) with Pandora spectrometer measurements for the 4 NYC  
 350 sites. The mean difference between OMPS and Pandora retrievals shows OMPS  
 351 ubiquitously underestimates in the NYC region from  $-6.0 \times 10^{15}$  (Queens NY) to  $-2.8 \times$   
 352  $10^{15}$  (Bronx NY) molecules/cm<sup>2</sup> (Figure 5). Outside of the NYC metro area, the average  
 353 OMPS column NO<sub>2</sub> is generally higher than or close to Pandoras, with the mean  
 354 difference between  $-0.3 \times 10^{15}$  (Richmond CA) and  $2.7 \times 10^{15}$  (New Brunswick NJ)  
 355 molecules/cm<sup>2</sup>, except for New Haven CT, which OMPS underestimates with an average  
 356 difference of  $-1.1 \times 10^{15}$  molecules/cm<sup>2</sup> from Pandora (Figure 5). To assess the statistical

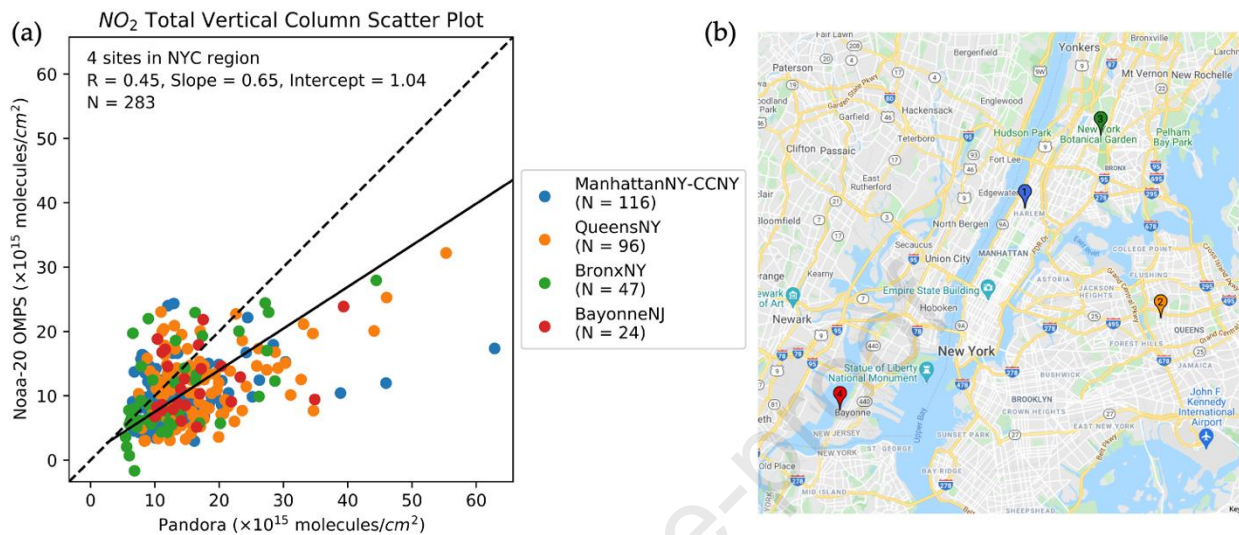
357 distribution of the OMPS biases, we plot the column NO<sub>2</sub> difference and percent  
358 difference as a function of pollution levels in Figure 6. For the least polluted columns (<  
359  $3 \times 10^{15}$  molecules/cm<sup>2</sup>), the inter-quantile range of column difference is 0.6 to  $4.5 \times$   
360  $10^{15}$ , with a median of  $3.3 \times 10^{15}$  molecules/cm<sup>2</sup>. When pollution level increases, the  
361 median difference gradually shifts from positive towards negative. For the more polluted  
362 columns (12 - 15 and  $> 15 \times 10^{15}$  molecules/cm<sup>2</sup>), the inter-quantile range of column  
363 differences are both in the negative range, with a median difference of -4 and  $-10 \times 10^{15}$   
364 molecules/cm<sup>2</sup>, respectively. Considering all data points from 13 sites during the 15-  
365 month validation span (N = 1434), the median difference and relative difference between  
366 NOAA-20 OMPS and Pandora are  $-0.1 \times 10^{15}$  molecules/cm<sup>2</sup> and -1% respectively, with  
367 an inter-quantile range of -2.8 to  $2.9 \times 10^{15}$  molecules/cm<sup>2</sup> and -32% to 44% respectively  
368 (Figure 6). The overall linear correlation between NOAA-20 and Pandora total columns  
369 is 0.40 and the correlation is higher ( $r = 0.43$ ) at higher pollution levels (Table 2). The  
370 quality of statistics of NOAA-20 OMPS is reasonably comparable to other satellite  
371 instrument bias with regard to Pandora measurements, see Text S1 for details (Herman et  
372 al., 2019; Ialongo et al., 2020, 2016; Judd et al., 2019; Lamsal et al., 2014).

373 These results from multiple Pandora spectrometer instruments indicate that OMPS NO<sub>2</sub>  
374 total columns underestimate for relatively large Pandora NO<sub>2</sub> total columns,  
375 corresponding to polluted urban regions and episodes of elevated pollution, while  
376 overestimate for relatively small NO<sub>2</sub> total columns. The low bias (OMPS  
377 underestimation) can be partially attributed to the sampling mismatch in spatial  
378 representativity between a point measurement from the ground-based spectrometer and  
379 an area-averaged quantity from the satellite iFOV (instantaneous Field of View, i.e.,



380 pixel). As the more polluted NO<sub>2</sub> columns observed by Pandora are likely occurring over  
381 spatial scales much smaller than the satellite resolutions, the satellite-to-Pandora linear  
382 relationship progressively worsens with increasing satellite pixel size, simply resulting  
383 from the flattening of higher NO<sub>2</sub> enhancement over larger spatial areas (Judd et al.,  
384 2019). Such behavior is more often associated with localized heterogeneous features  
385 rather than more well mixed regional-scale enhancements. In addition, because of the  
386 relatively coarse resolution of the OMPS a priori profiles, OMPS tropospheric columns  
387 are expected to have a low bias over polluted areas where the actual peak in the NO<sub>2</sub>  
388 profiles is close to the surface, and the boundary layer column is underestimated in the a  
389 priori. Similarly, the less polluted columns could be overestimated due to a slightly  
390 overestimate of boundary layer NO<sub>2</sub>, resulting from the averaging effect of low-  
391 resolution a priori profiles in situations of large spatial heterogeneity. Replacing the  
392 coarse ( $1^\circ \times 1.25^\circ$ ) a priori NO<sub>2</sub> profiles with high-resolution profiles from chemical

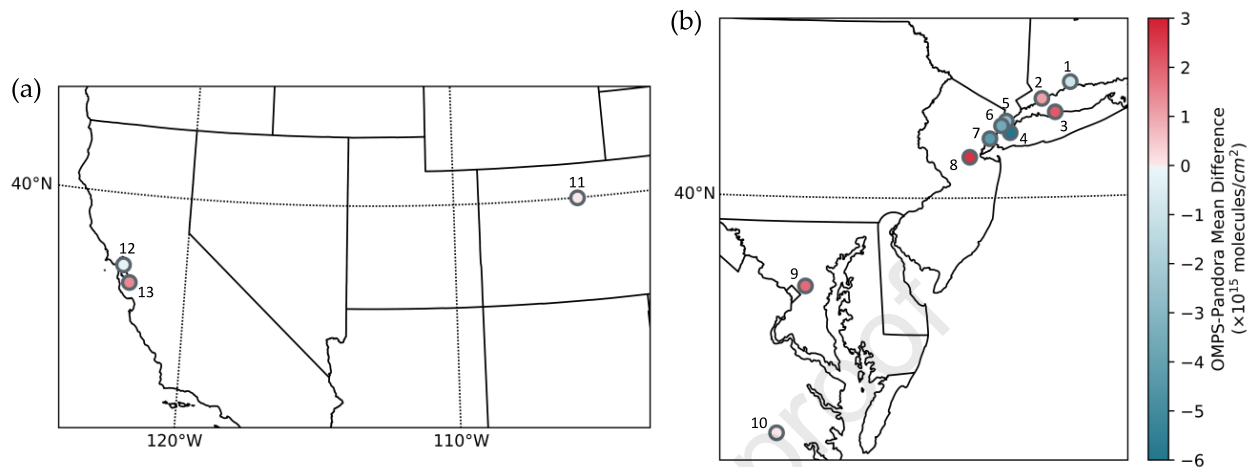
393 transport models can potentially improve the agreement between NOAA-20 OMPS and  
 394 Pandora.



395

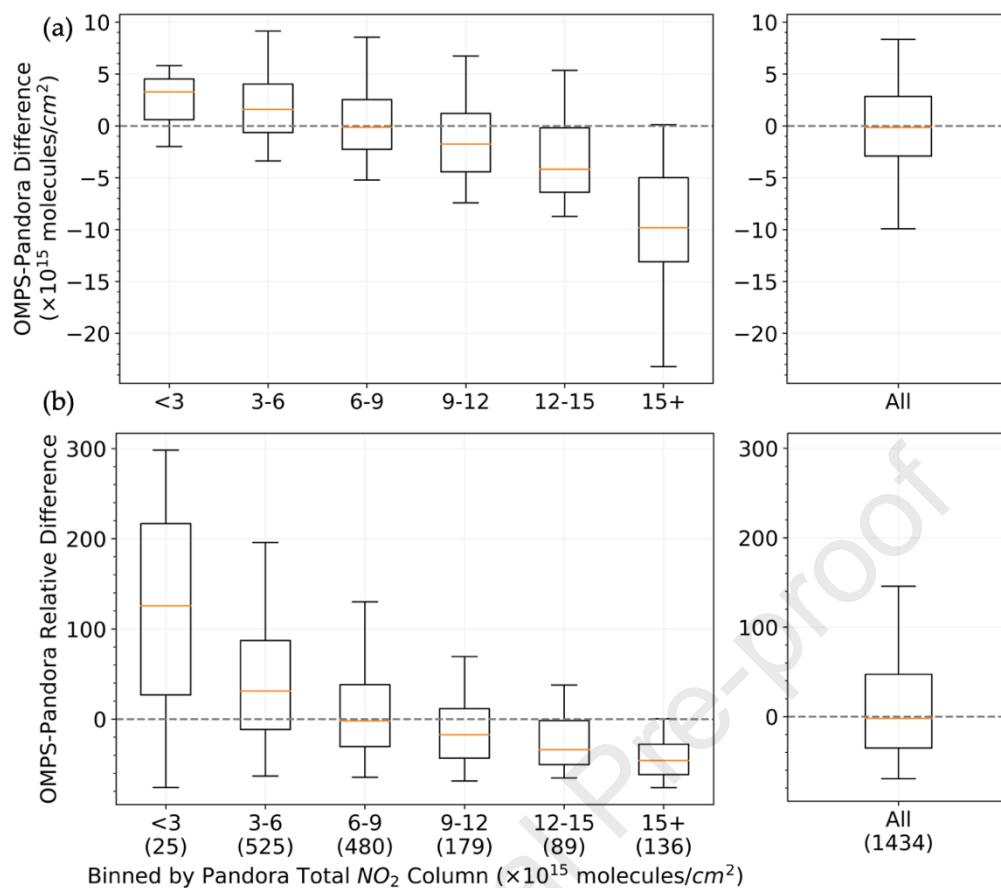
396 **Figure 4.** (a) Scatter plot of NOAA-20 OMPS and Pandora observed  $NO_2$  total vertical columns  
 397 over 4 ground stations in New York metropolitan area, from 2019-02-14 to 2020-04-30. The  
 398 statistics of linear regression fit are shown on the plot (N represents the number of coincidences).  
 399 Note that different stations have different date spans and thus different number of coincidences  
 400 with OMPS, coincidence by station is shown in the legend; (b) The locations of 4 stations on

401 Google Map, the color of each station on the map corresponds to the color used in the scatter  
 402 plot.



403 1 NewHavenCT, 2 WestportCT, 3 OldFieldNY, 4 QueensNY, 5 BronxNY, 6 ManhattanNY-CCNY, 7 BayonneNJ, 8 NewBrunswickNJ,  
 9 GreenbeltMD, 10 CharlesCityVA, 11 BoulderCO, 12 RichmondCA, 13 MountainViewCA

404 **Figure 5.** Locations of Pandora ground stations over (a) western U.S. (3 stations) and (b) eastern  
 405 U.S. (10 stations), colored by the average difference between OMPS and Pandora measured total  
 406 NO<sub>2</sub> columns.



407

408 **Figure 6.** Box-whisker plots (95-75-50-25-5 percentiles) showing the (a) absolute difference and  
 409 (b) relative difference between NOAA-20 OMPS and Pandora measured total NO<sub>2</sub> columns,  
 410 binned by Pandora columns at the labeled thresholds (left), as well as all data points (right). The  
 411 number of points in each bin and all data are indicated by the numbers in parentheses. The data

412 used in the analysis are collected from the 13 U.S. Pandora stations as shown in Figure 5, over a  
 413 period from 2019-02-14 to 2020-04-30.

414 **Table 2.** Statistics of the comparison between NOAA-20 OMPS and Pandora NO<sub>2</sub> total columns,  
 415 based on all data from 13 U.S. Pandora stations during 2019-02-14 to 2020-04-30. The  
 416 uncertainties are the corresponding standard errors of the mean.

	Mean relative difference <sup>a</sup>	Mean difference <sup>b</sup>	Standard deviation of absolute bias <sup>c</sup>	r <sup>d</sup>	slope <sub>OLS</sub> <sup>e</sup>	slope <sub>RMA</sub> <sup>f</sup>	N <sup>g</sup>
All data	14.8 ± 2.0	-0.29 ± 0.15	5.8	0.40	0.32	0.81	1434
Pandora high <sup>h</sup>	-34.6 ± 2.1	-7.18 ± 0.49	7.4	0.43	0.29	0.72	225
Pandora low <sup>i</sup>	24.1 ± 2.2	1.00 ± 0.12	4.3	0.20	0.38	1.95	1209

417 <sup>a</sup> Mean relative difference (%). <sup>b</sup> Mean difference ( $\times 10^{15}$  molecules/cm<sup>2</sup>). <sup>c</sup> Standard deviation of column difference  
 418 ( $\times 10^{15}$  molecules/cm<sup>2</sup>). <sup>d</sup> Correlation coefficient. <sup>e</sup> Least squares linear fit slope. <sup>f</sup> Reduced major axis linear fit  
 419 slope. <sup>g</sup> Number of coincidences. <sup>h</sup> Pandora NO<sub>2</sub> total columns  $\geq 12 \times 10^{15}$  molecules/cm<sup>2</sup>. <sup>i</sup> Pandora NO<sub>2</sub> total  
 420 columns  $< 12 \times 10^{15}$  molecules/cm<sup>2</sup>.

421

### 422 3.4 Tropospheric NO<sub>2</sub> column reductions during COVID-19

423 In this section, we demonstrate the high sensitivity of NOAA-20 OMPS NO<sub>2</sub>  
 424 observations with COVID-19 application and quantify the impact of COVID-19 outbreak  
 425 on global NO<sub>2</sub> pollution. During the early half of 2020, many countries around the world  
 426 enforced physical distancing measures in response to the outbreak of the COVID-19  
 427 crisis (Table S1). China's policy interventions are among the most stringent. Figure 7  
 428 shows a visual comparison of OMPS observed tropospheric NO<sub>2</sub> columns over China  
 429 before and after the lockdown in 2020 (a-e) and over the same period in 2021 (f-j), with

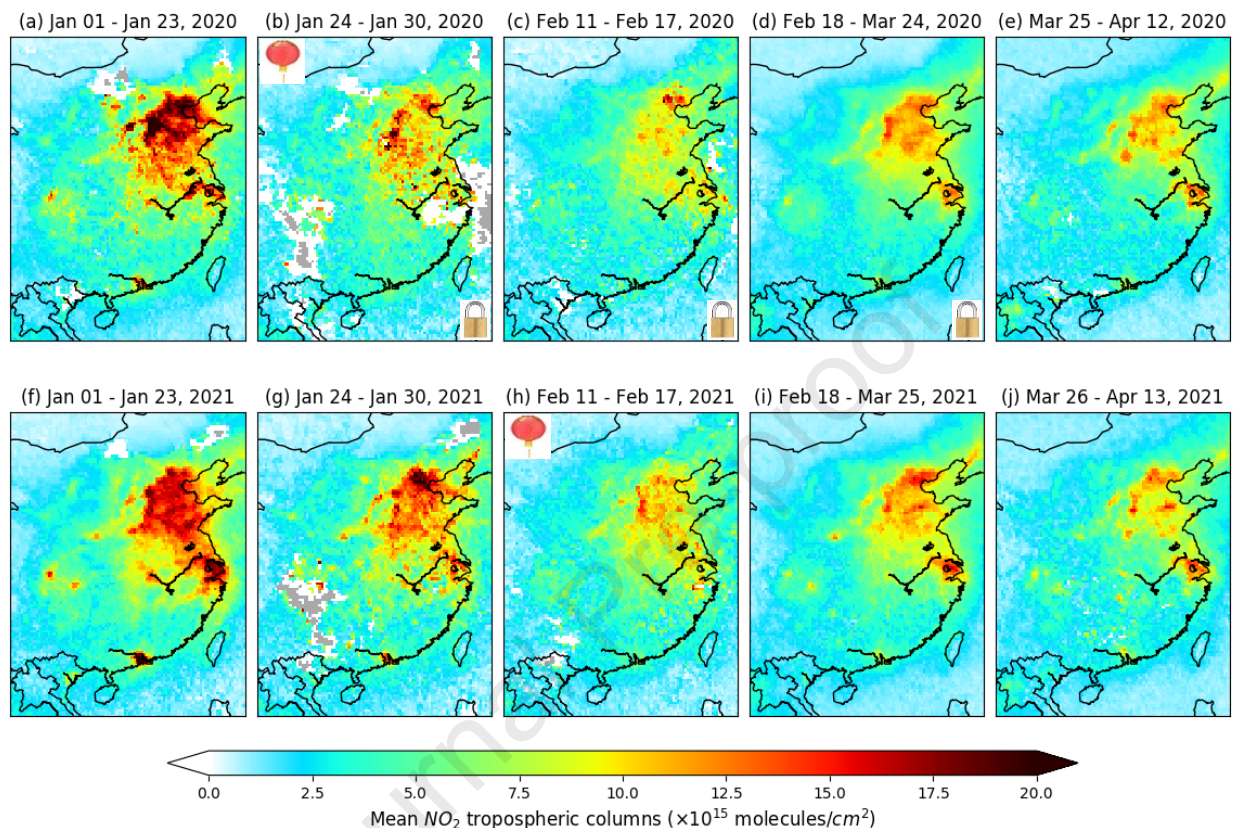
430 indications of the Chinese New Year holiday (by red lantern, top left) and of the  
431 lockdown period (by padlock, bottom right). In 2021, OMPS observed large winter NO<sub>2</sub>  
432 abundances (Figure 7f-g) followed by a drop during the Chinese New Year holiday  
433 (CNY hereafter, Figure 7h). The NO<sub>2</sub> TVCDs decline during CNY is a typical  
434 phenomenon observed every year because most Chinese factories shut down for the  
435 holiday and the traffic volumes decrease, resulting in a decrease in fuel consumption and  
436 thus NO<sub>x</sub> emissions. A rebound of NO<sub>2</sub> TVCDs is usually observed right after CNY,  
437 marking the end of the 7-day CNY holiday and people get back to work (Figure 7i). Note  
438 that the NO<sub>2</sub> rebound after CNY is much lower than its January peak, due to seasonality  
439 caused by shorter NO<sub>2</sub> lifetime in the warmer season. In 2020, since the initial phase  
440 lockdown is coincident with the CNY holiday, NO<sub>x</sub> emissions curtail significantly and  
441 NOAA-20 OMPS observations indicate a steep drop of NO<sub>2</sub> TVCDs, reaching a factor of  
442 2 or more at most Chinese cities (Figure 7b). The average NO<sub>2</sub> reduction in 2020 over  
443 China is 35% from “before” (Figure 7a) to “after” (Figure 7b), while a reduction of 15%  
444 in 2021 is observed. This suggests that the observed reduction in 2020 far exceeds the  
445 typical holiday-related reduction. In addition, unlike the typical years that we see a clear  
446 NO<sub>2</sub> reduction during and a quick increase after CNY, NO<sub>2</sub> columns do not bounce back  
447 after the week of 2020 CNY holiday (Figure 7c). In fact, it remains low for several weeks  
448 during strict COVID-19 quarantine (31 Jan – 17 Feb 2020), after which NO<sub>2</sub> columns  
449 gradually recover, reflecting the return of economic activities and NO<sub>x</sub> emissions (Figure  
450 7d-e).

451 A quantitative analysis of the impact of the COVID-19 measures on NO<sub>2</sub> in China as well  
452 as in other countries is given in Table 3. Note that the relatively large and not fully

453 understood contribution of background NO<sub>2</sub> columns has a large impact on trend analyses  
454 as more background signal is incorporated into the analysis, whether by incorporating a  
455 large spatial area or by computing the analysis over less polluted cities (Qu et al., 2021;  
456 Silvern et al., 2019). We compare the observed NO<sub>2</sub> TVCDs during the lockdown in 2020  
457 versus a recovering year NO<sub>2</sub> in 2021. This year-over-year comparison calculates NO<sub>2</sub>  
458 column averages starting on the same reference date and last for 21 days, to exclude  
459 seasonality-caused NO<sub>2</sub> changes. For the Chinese cities in Table 3, we averaged NO<sub>2</sub>  
460 TVCDs between 31 January and 10 February 2020 (11 days) compared to the same  
461 period in 2021, in order to eliminate the interference of CNY holidays. Similarly, the  
462 lockdown period for Iran was chosen between 4 March and 19 March (16 days) to  
463 eliminate the interference of the Nowruz holiday. Substantial NO<sub>2</sub> column reductions in  
464 2020 (relative to 2021) are evident in many cities around the world where strict COVID-  
465 19 precautions were enforced. The observed column decreases are largely due to the  
466 decline of traffic emissions, by far the dominant NO<sub>x</sub> emission source in cities, as well as  
467 decreases in industrial activities and power generation (Myllyvirta, 2020; Schuman,  
468 2020; Zara, 2020). Simulations of chemistry transport models are needed if to isolate the  
469 benefit of emission reduction from variations of transport (Valin et al., 2013) or NO<sub>x</sub>  
470 lifetime (Laughner and Cohen, 2019). Note that since we are comparing 2020 NO<sub>2</sub>  
471 columns to 2021, part of the lockdown related NO<sub>2</sub> reduction might be canceled out by  
472 the lower emission rate in 2021 due to the emission declines benefited from  
473 environmental regulations with each advancing year (Wu et al., 2019). Therefore, the



474 actual NO<sub>2</sub> decreases could be larger if we were to compare with 2019 NO<sub>2</sub>, as shown in  
 475 the TROPOMI study of (Bauwens et al., 2020) Table 1.



476

477 **Figure 7.** Mean tropospheric NO<sub>2</sub> columns over China as observed by NOAA-20 OMPS  
 478 (a) before and (b-e) after the COVID-19 lockdowns. For the comparison, the same time  
 479 periods are shown for 2021 (f-j). The Chinese New Year holiday covers the weeks of Jan  
 480 24-30 in 2020 and Feb 11-17 in 2021, which are indicated by the red lanterns in panel (b)  
 481 and (h). The lockdown measures are initiated during and extended after the 2020 Chinese  
 482 New Year holiday, shown by the padlock sign in panel (b-d), and partial loosening of the



483 restrictions starting Mar 25, 2020, shown in panel (e). Grey areas on the maps indicate no  
 484 valid data due to the 30% cloud fraction filter.

485

486 **Table 3.** NO<sub>2</sub> TCVDs reduction observed during the COVID-19 lockdown period, starting on  
 487 the Reference date and lasting for 21 days, relative to the same period in 2021, with the  
 488 exception of China and Iran, where it lasts for 11 and 16 days respectively, in order to avoid the  
 489 interference with the New Year Holidays. The percentage change is defined as  $(TVCD_{s2020} -$   
 490  $TVCD_{s2021})/TVCD_{s2021} \times 100\%$ . The numbers in the brackets are standard error of the mean.

City	Lat	Lon	Reference date	NOAA-20 OMPS
Beijing	39.9	116.4	31-Jan-20	-27(±4)%
Tianjin	39.3	117.4	31-Jan-20	-33(±3)%
Shenyang	41.8	123.4	31-Jan-20	-21(±4)%
Zhengzhou	34.7	113.6	31-Jan-20	-29(±3)%
Jinan	36.7	117.1	31-Jan-20	-46(±3)%
Shanghai	31.2	121.5	31-Jan-20	3(±7)%
Chengdu	30.6	104.1	31-Jan-20	-50(±6)%
Guangzhou	23.1	113.3	31-Jan-20	-68(±3)%
Shenzhen	22.5	114.1	31-Jan-20	-56(±4)%
Hong Kong	22.3	114.2	31-Jan-20	-54(±4)%
New Delhi	28.6	77.2	25-Mar-20	-16(±2)%
Mumbai	19.1	72.9	25-Mar-20	-12(±4)%
Milan	45.5	9.2	23-Feb-20	-23(±4)%
Venice	45.4	12.3	23-Feb-20	-16(±4)%
Madrid	40.4	3.7	15-Mar-20	-32(±3)%
Barcelona	41.4	2.2	15-Mar-20	-15(±4)%
Moscow	55.8	37.6	30-Mar-20	-37(±3)%
Tehran	35.7	51.4	04-Mar-20	12(±7)%

New York	40.7	-74.0	24-Mar-20	-22( $\pm$ 4)%
Washington DC	38.9	-77.0	24-Mar-20	-18( $\pm$ 4)%
Chicago	41.9	-87.6	24-Mar-20	-17( $\pm$ 4)%

491

492 Note: We used OMPS global daily gridded Level-3 data at  $0.25^\circ \times 0.25^\circ$  and the reductions are  
 493 calculated based on pixels within a 100-km radius around the city center with cloud fractions of  
 494 40% or less.

495

#### 496 **4 Summary**

497 In this work, we have presented a suite of product development behind the new NOAA-20  
 498 OMPS tropospheric NO<sub>2</sub> columns, covering retrieval algorithm, validation, and application  
 499 during COVID-19. We applied the advanced DVCF algorithm and effective STS approach to  
 500 UV measurements from NOAA-20/OMPS NM, which were successfully used to retrieve NO<sub>2</sub>  
 501 from its predecessors: SNPP/OMPS and Aura/OMI.

502 To evaluate NOAA-20 OMPS NO<sub>2</sub> column retrievals, we first compared the stratospheric NO<sub>2</sub>  
 503 vertical columns derived from OMPS to those from OMI. The comparison shows excellent  
 504 agreement in detecting the stratospheric background columns between the two instruments,  
 505 which facilitates the accuracy of the remained OMPS tropospheric NO<sub>2</sub> retrievals. The result also  
 506 validates the sliding-median STS scheme that is adopted in NOAA-20 OMPS, especially given  
 507 the agreement relies on independent spectral measurements at different wavelengths using very  
 508 different retrieval methods. We compared NOAA-20 OMPS with OMI monthly mean TVCDs  
 509 observations for December 2019. It shows similar spatial distributions and good quantitative  
 510 agreement. We then preliminarily validated OMPS NO<sub>2</sub> columns against the independent NO<sub>2</sub>  
 511 measurements from 4 ground-based Pandora spectrometers over the NYC metro area. NOAA-20

512 NO<sub>2</sub> observations biased low against (-28%) and are moderately correlated ( $r = 0.45$ ) with  
513 Pandora total columns. The evaluation was then extended to other U.S. Pandora stations, with a  
514 total of 13 stations compared with NOAA-20 OMPS. The results suggest that OMPS NO<sub>2</sub> total  
515 columns underestimate for relatively large Pandora NO<sub>2</sub> total columns, corresponding to polluted  
516 urban regions and episodes of elevated pollution, while overestimate for relatively small NO<sub>2</sub>  
517 total columns. Part of the low biases is expected and can be explained by spatial representativity  
518 mismatch between satellite and ground-based measurements, when an area-averaged quantity  
519 over relatively large satellite pixel is compared with Pandora observations that have small FOV.  
520 Such kind of spatial representativity mismatch is often associated with localized large pollution  
521 enhancements observed by Pandora and OMPS is spatially averaged with nearby less-polluted  
522 locations within the larger satellite pixel area. Other than that, the biases (both underestimation  
523 and overestimation) are possibly caused by the coarse a priori profiles currently used in the  
524 NOAA-20 NO<sub>2</sub> retrievals. Replacing the a priori NO<sub>2</sub> profiles from high-resolution chemical  
525 transport models could potentially improve the agreement. Finally, with the new NOAA-20  
526 OMPS NO<sub>2</sub> retrievals, we investigated the impact of COVID-19 lockdown on urban NO<sub>2</sub> air  
527 pollution. It shows a 20-40% drastic decline in tropospheric NO<sub>2</sub> around the world in January-  
528 April 2020 during COVID-19 precautions, supporting the analyses from other satellite-based  
529 studies (Bauwens et al., 2020; Goldberg et al., 2020; Liu et al., 2020). These results demonstrate  
530 the high sensitivity of NOAA-20 OMPS to tropospheric NO<sub>2</sub> and validate its potential use for  
531 extending the long-term global NO<sub>2</sub> record on the series of OMPS-NMs aboard JPSS satellites.

532

533 **Author Contributions Statement**

534 **Xinzhou Huang**: Conceptualization, Data curation, Formal analysis, Investigation,  
535 Methodology, Software, Validation, Visualization, Roles/Writing - original draft, Writing -  
536 review & editing. **Kai Yang**: Conceptualization, Data curation, Funding acquisition,  
537 Methodology, Project administration, Resources, Software, Supervision, Writing - review &  
538 editing. **Shobha Kondragunta**: Project administration; Resources; Supervision; Writing -  
539 review & editing. **Zigang Wei**: Investigation. **Lucas Valin**: Resources, Writing - review &  
540 editing. **James Szykman**: Resources, Supervision, Writing - review & editing. **Mitch Goldberg**:  
541 Project administration, Resources, Supervision.

542

#### 543 **Disclaimer**

544 The authors declare no conflict of interest. The scientific results and conclusions, as well as any  
545 views or opinions expressed herein, are those of the author(s) and do not necessarily reflect those  
546 of EPA, NOAA, or the Department of Commerce.

547

#### 548 **Data Availability Statement**

549 The NOAA-20 OMPS NO<sub>2</sub> data can be obtained at <https://umd.box.com/v/n20-omps-no2>.  
550 Pandora data are located at <http://data.pandonia-global-network.org/>, and OMI L2 NO<sub>2</sub> data at  
551 [https://disc.gsfc.nasa.gov/datasets/OMNO2\\_003/summary](https://disc.gsfc.nasa.gov/datasets/OMNO2_003/summary).

552

#### 553 **Acknowledgement**

554 This work was supported by the U.S. National Oceanic and Atmospheric Administration

555 (NOAA) [grant number: NA19NES4320002]. We acknowledge the JPSS project for providing  
 556 the OMPS L1 data used in this study.

557

## 558 References

- 559 Bauwens, M., Compernelle, S., Stavrou, T., Müller, J.F., van Gent, J., Eskes, H., Levelt, P.F.,  
 560 van der A, R., Veefkind, J.P., Vlietinck, J., Yu, H., Zehner, C., 2020. Impact of Coronavirus  
 561 Outbreak on NO<sub>2</sub> Pollution Assessed Using TROPOMI and OMI Observations. *Geophys.*  
 562 *Res. Lett.* 47, 1–9. <https://doi.org/10.1029/2020GL087978>
- 563 Beirle, S., Boersma, K.F., Platt, U., Lawrence, M.G., Wagner, T., 2011. Megacity emissions and  
 564 lifetimes of nitrogen oxides probed from space. *Science* (80-. ). 333, 1737–1739.  
 565 <https://doi.org/10.1126/SCIENCE.1207824>
- 566 Beirle, S., Borger, C., Dörner, S., Li, A., Hu, Z., Liu, F., Wang, Y., Wagner, T., 2019.  
 567 Pinpointing nitrogen oxide emissions from space. *Sci. Adv.* 5, 1–7.  
 568 <https://doi.org/10.1126/sciadv.aax9800>
- 569 Boersma, K.F., Eskes, H.J., Veefkind, J.P., Brinksma, E.J., Van Der A, R.J., Sneep, M., Van Den  
 570 Oord, G.H.J., Levelt, P.F., Stammes, P., Gleason, J.F., Bucsela, E.J., 2007. Near-real time  
 571 retrieval of tropospheric NO<sub>2</sub> from OMI. *Atmos. Chem. Phys.* 7, 2103–2118.  
 572 <https://doi.org/10.5194/acp-7-2103-2007>
- 573 Brodzik, M. J., Stewart, J. S., 2021. Near-Real-Time SSM/I-SSMIS EASE-Grid Daily Global  
 574 Ice Concentration and Snow Extent, Version 3 [Data Set]. Boulder, Colorado USA. NASA  
 575 National Snow and Ice Data Center Distributed Active Archive Center.  
 576 <https://doi.org/10.5067/JAQDJKPX0S60>. Date Accessed 08-09-2022.
- 577 Duncan, B.N., Lamsal, L.N., Thompson, A.M., Yoshida, Y., Lu, Z., Streets, D.G., Hurwitz,  
 578 M.M., Pickering, K.E., 2016. A space-based, high-resolution view of notable changes in  
 579 urban NO<sub>x</sub> pollution around the world (2005–2014). *J. Geophys. Res.* 121, 976–996.  
 580 <https://doi.org/10.1002/2015JD024121>
- 581 ESA, 2020. Air pollution drops in India following lockdown. *Eur. Sp. Agency* 1–5.
- 582 Goldberg, D.L., Anenberg, S.C., Griffin, D., McLinden, C.A., Lu, Z., Streets, D.G., 2020.  
 583 Disentangling the Impact of the COVID-19 Lockdowns on Urban NO<sub>2</sub> From Natural  
 584 Variability. *Geophys. Res. Lett.* 47. <https://doi.org/10.1029/2020GL089269>
- 585 Herman, J., Abuhassan, N., Kim, Jhoon, Kim, Jae, Dubey, M., Raponi, M., Tzortziou, M., 2019.  
 586 Underestimation of column NO<sub>2</sub> amounts from the OMI satellite compared to diurnally  
 587 varying ground-based retrievals from multiple PANDORA spectrometer instruments.  
 588 *Atmos. Meas. Tech.* 12, 5593–5612. <https://doi.org/10.5194/amt-12-5593-2019>
- 589 Huang, G., Sun, K., 2020. Non-negligible impacts of clean air regulations on the reduction of  
 590 tropospheric NO<sub>2</sub> over East China during the COVID-19 pandemic observed by OMI and  
 591 TROPOMI. *Sci. Total Environ.* 745, 141023.  
 592 <https://doi.org/10.1016/j.scitotenv.2020.141023>
- 593 Ialongo, I., Herman, J., Krotkov, N., Lamsal, L., Folkert Boersma, K., Hovila, J., Tamminen, J.,  
 594 2016. Comparison of OMI NO<sub>2</sub> observations and their seasonal and weekly cycles with  
 595 ground-based measurements in Helsinki. *Atmos. Meas. Tech.* 9, 5203–5212.

- 596 <https://doi.org/10.5194/amt-9-5203-2016>
- 597 Ialongo, I., Virta, H., Eskes, H., Hovila, J., Douros, J., 2020. Comparison of  
598 TROPOMI/Sentinel-5 Precursor NO<sub>2</sub> observations with ground-based measurements in  
599 Helsinki. *Atmos. Meas. Tech.* 13, 205–218. <https://doi.org/10.5194/amt-13-205-2020>
- 600 Judd, L.M., Al-Saadi, J.A., Janz, S.J., Kowalewski, M.J.G., Bradley Pierce, R., Szykman, J.J.,  
601 Valin, L.C., Swap, R., Cede, A., Mueller, M., Tiefengraber, M., Abuhassan, N., Williams,  
602 D., 2019. Evaluating the impact of spatial resolution on tropospheric NO<sub>2</sub> column  
603 comparisons within urban areas using high-resolution airborne data. *Atmos. Meas. Tech.*  
604 12, 6091–6111. <https://doi.org/10.5194/amt-12-6091-2019>
- 605 Judd, L.M., Al-Saadi, J.A., Szykman, J.J., Valin, L.C., Janz, S.J., Kowalewski, M.G., Eskes,  
606 H.J., Pepijn Veefkind, J., Cede, A., Mueller, M., Gebetsberger, M., Swap, R., Bradley  
607 Pierce, R., Nowlan, C.R., González Abad, G., Nehrir, A., Williams, D., 2020. Evaluating  
608 Sentinel-5P TROPOMI tropospheric NO<sub>2</sub> column densities with airborne and Pandora  
609 spectrometers near New York City and Long Island Sound. *Atmos. Meas. Tech.* 13, 6113–  
610 6140. <https://doi.org/10.5194/AMT-13-6113-2020>
- 611 Judd, L.M., Al-Saadi, J.A., Valin, L.C., Bradley Pierce, R., Yang, K., Janz, S.J., Kowalewski,  
612 M.G., Szykman, J.J., Tiefengraber, M., Mueller, M., 2018. The dawn of geostationary air  
613 quality monitoring: Case studies from Seoul and Los Angeles. *Front. Environ. Sci.* 6.  
614 <https://doi.org/10.3389/fenvs.2018.00085>
- 615 Kleipool, Q.L., Dobber, M.R., de Haan, J.F., Levelt, P.F., 2008. Earth surface reflectance  
616 climatology from 3 years of OMI data. *J. Geophys. Res. Atmos.* 113, 18308.  
617 <https://doi.org/10.1029/2008JD010290>
- 618 Kondragunta, S., Wei, Z., McDonald, B.C., Goldberg, D.L., Tong, D.Q., 2021. COVID-19  
619 Induced Fingerprints of a New Normal Urban Air Quality in the United States. *J. Geophys.*  
620 *Res. Atmos.* 126, e2021JD034797. <https://doi.org/10.1029/2021JD034797>
- 621 Lamsal, L.N., Krotkov, N.A., Celarier, E.A., Swartz, W.H., Pickering, K.E., Bucsela, E.J.,  
622 Gleason, J.F., Martin, R. V., Philip, S., Irie, H., Cede, A., Herman, J., Weinheimer, A.,  
623 Szykman, J.J., Knepp, T.N., 2014. Evaluation of OMI operational standard NO<sub>2</sub> column  
624 retrievals using in situ and surface-based NO<sub>2</sub> observations. *Atmos. Chem. Phys.* 14,  
625 11587–11609. <https://doi.org/10.5194/acp-14-11587-2014>
- 626 Laughner, J.L., Cohen, R.C., 2019. Direct observation of changing NO<sub>x</sub> lifetime in North  
627 American cities. *Science (80- )*. 366, 723–727. <https://doi.org/10.1126/science.aax6832>
- 628 Lelieveld, J., Evans, J.S., Fnais, M., Giannadaki, D., Pozzer, A., 2015. The contribution of  
629 outdoor air pollution sources to premature mortality on a global scale. *Nature* 525, 367–371.  
630 <https://doi.org/10.1038/nature15371>
- 631 Lin, N., Wang, Y., Zhang, Y., Yang, K., 2019. A large decline of tropospheric NO<sub>2</sub> in China  
632 observed from space by SNPP OMPS. *Sci. Total Environ.* 675, 337–342.  
633 <https://doi.org/10.1016/j.scitotenv.2019.04.090>
- 634 Liu, F., Page, A., Strode, S.A., Yoshida, Y., Choi, S., Zheng, B., Lamsal, L.N., Li, C., Krotkov,  
635 N.A., Eskes, H., Ronald van der, A., Veefkind, P., Levelt, P.F., Hauser, O.P., Joiner, J.,  
636 2020. Abrupt decline in tropospheric nitrogen dioxide over China after the outbreak of  
637 COVID-19. *Sci. Adv.* 6, 1–10. <https://doi.org/10.1126/sciadv.abc2992>
- 638 Myllyvirta, L., 2020. Analysis: Coronavirus temporarily reduced China's CO<sub>2</sub> emissions by a  
639 quarter [WWW Document]. *Carbonbrief*. URL [https://www.carbonbrief.org/analysis-](https://www.carbonbrief.org/analysis-coronavirus-has-temporarily-reduced-chinas-co2-emissions-by-a-quarter)  
640 [coronavirus-has-temporarily-reduced-chinas-co2-emissions-by-a-quarter](https://www.carbonbrief.org/analysis-coronavirus-has-temporarily-reduced-chinas-co2-emissions-by-a-quarter) (accessed  
641 10.2.21).



- 642 Qu, Z., Jacob, D.J., Silvern, R.F., Shah, V., Campbell, P.C., Valin, L.C., Murray, L.T., 2021. US  
643 COVID-19 Shutdown Demonstrates Importance of Background NO<sub>2</sub> in Inferring NO<sub>x</sub>  
644 Emissions From Satellite NO<sub>2</sub> Observations. *Geophys. Res. Lett.* 48, 1–8.  
645 <https://doi.org/10.1029/2021GL092783>
- 646 Rivas, M.B., Veefkind, P., Boersma, F., Levelt, P., Eskes, H., Gille, J., 2014. Intercomparison of  
647 daytime stratospheric NO<sub>2</sub> satellite retrievals and model simulations. *Atmos. Meas. Tech.* 7,  
648 2203–2225. <https://doi.org/10.5194/amt-7-2203-2014>
- 649 Schuman, R., 2020. INRIX U.S. National Traffic Volume Synopsis [WWW Document]. INRIX.  
650 URL <https://inrix.com/blog/covid19-us-traffic-volume-synopsis/> (accessed 10.2.21).
- 651 Seinfeld, J.H., Pandis, S.N., 2016. *Atmospheric Chemistry and Physics: From Air Pollution to*  
652 *Climate Change*, 3rd Edition | Wiley.
- 653 Shah, V., Jacob, D., Li, K., Silvern, R., Zhai, S., Liu, M., Lin, J., Zhang, Q., 2020. Effect of  
654 changing NO<sub>x</sub> lifetime on the seasonality and long-term trends of satellite-observed  
655 tropospheric NO<sub>2</sub> columns over China. *Atmos. Chem. Phys.* 20, 1483–1495.  
656 <https://doi.org/10.5194/acp-20-1483-2020>
- 657 Silvern, R.F., Jacob, D.J., Mickley, L.J., Sulprizio, M.P., Travis, K.R., Marais, E.A., Cohen,  
658 R.C., Laughner, J.L., Choi, S., Joiner, J., 2019. Using satellite observations of tropospheric  
659 NO<sub>2</sub> columns to infer long-term trends in US NO<sub>x</sub> emissions: the importance of accounting  
660 for the free tropospheric NO<sub>2</sub> background 19, 1–16. [https://doi.org/10.5194/acp-19-8863-](https://doi.org/10.5194/acp-19-8863-2019)  
661 [2019](https://doi.org/10.5194/acp-19-8863-2019)
- 662 Solomon, S., Garcia, R.R., 1983. On the distribution of nitrogen dioxide in the high-latitude  
663 stratosphere. *J. Geophys. Res. Ocean.* 88, 5229–5239.  
664 <https://doi.org/10.1029/JC088IC09P05229>
- 665 Tzortziou, M., Kwong, C.F., Goldberg, D., Schiferl, L., Commane, R., Abuhassan, N., Szykman,  
666 J., Valin, L., 2021. Declines and peaks in NO<sub>2</sub>; pollution during the  
667 multiple waves of the COVID-19 pandemic in the New York metropolitan area. *Atmos.*  
668 *Chem. Phys. Discuss.* 1–30. <https://doi.org/10.5194/acp-2021-592>
- 669 Valin, L.C., Russell, A.R., Bucsela, E.J., Veefkind, J.P., Cohen, R.C., 2011. Observation of slant  
670 column NO<sub>2</sub> using the super-zoom mode of AURA-OMI. *Atmos. Meas. Tech.* 4, 1929–  
671 1935. <https://doi.org/10.5194/amt-4-1929-2011>
- 672 Valin, L.C., Russell, A.R., Cohen, R.C., 2013. Variations of OH radical in an urban plume  
673 inferred from NO<sub>2</sub> column measurements. *Geophys. Res. Lett.* 40, 1856–1860.  
674 <https://doi.org/10.1002/GRL.50267>
- 675 Wu, R., Liu, F., Tong, D., Zheng, Y., Lei, Y., Hong, C., Li, M., Liu, J., Zheng, B., Bo, Y., Chen,  
676 X., Li, X., Zhang, Q., 2019. Air quality and health benefits of China’s emission control  
677 policies on coal-fired power plants during 2005–2020. *Environ. Res. Lett.* 14, 094016.  
678 <https://doi.org/10.1088/1748-9326/ab3bae>
- 679 Yang, K., Carn, S.A., Ge, C., Wang, J., Dickerson, R.R., 2014. Advancing measurements of  
680 tropospheric NO<sub>2</sub> from space: New algorithm and first global results from OMPS.  
681 *Geophys. Res. Lett.* 41, 4777–4786. <https://doi.org/10.1002/2014GL060136>
- 682 Yang, K., Krotkov, N.A., Krueger, A.J., Carn, S.A., Bhartia, P.K., Levelt, P.F., 2009. Improving  
683 retrieval of volcanic sulfur dioxide from backscattered UV satellite observations L03102.  
684 *Geophys. Res. Lett.* 36, 1–5. <https://doi.org/10.1029/2008GL036036>
- 685 Yang, K., Krotkov, N.A., Krueger, A.J., Carn, S.A., Bhartia, P.K., Levelt, P.F., 2007. Retrieval  
686 of large volcanic SO<sub>2</sub> columns from the Aura Ozone Monitoring Instrument: Comparison  
687 and limitations. *J. Geophys. Res. Atmos.* 112. <https://doi.org/10.1029/2007JD008825>

- 688 Yang, K., Liu, X., 2019. Ozone Profile Climatology for Remote Sensing Retrieval Algorithms.  
689 Atmos. Meas. Tech. Discuss. 1–39. <https://doi.org/10.5194/amt-2019-116>
- 690 Zara, C., 2020. Watch flight traffic literally disappear from the skies as the coronavirus hits  
691 travel demand [WWW Document]. Fastcompany. URL  
692 [https://www.fastcompany.com/90473146/watch-flight-traffic-literally-disappear-from-the-](https://www.fastcompany.com/90473146/watch-flight-traffic-literally-disappear-from-the-skies-as-the-coronavirus-hits-travel-demand)  
693 [skies-as-the-coronavirus-hits-travel-demand](https://www.fastcompany.com/90473146/watch-flight-traffic-literally-disappear-from-the-skies-as-the-coronavirus-hits-travel-demand) (accessed 10.2.21).  
694

Journal Pre-proof



## Highlights

- Daily global NO<sub>2</sub> distribution can be mapped by NOAA-20 OMPS measurements.
- NOAA-20 OMPS detects a large decline (20 – 40%) of tropospheric NO<sub>2</sub> due to COVID-19 lockdown.
- OMPS tropospheric NO<sub>2</sub> correlates well with ground-based Pandora measurements.
- OMPS stratospheric NO<sub>2</sub> agrees excellently with OMI observations.

Journal Pre-proof

**Declaration of interests**

The authors declare that they have no known competing financial interests or personal relationships that could have appeared to influence the work reported in this paper.

The authors declare the following financial interests/personal relationships which may be considered as potential competing interests:

Journal Pre-proof